Chinese Journal of Chemical Engineering 90 (2026) 249–260

Contents lists available at ScienceDirect

Chinese Journal of Chemical Engineering

journal homepage: www.elsevier.com/locate/CJChE

Full Length Article

Experimental and modeling study of micromixing characteristics in a stirred tank integrated with annular jet flow

Guangshuo Wu , Ziqi Cai , Zhipeng Li , Junhao Wang *, Zhengming Gao *

State Key Laboratory of Chemical Resource Engineering, School of Chemical Engineering, Beijing University of Chemical Technology, Beijing 100029, China

ARTICLE INFO

Article history:
Received 31 July 2025
Received in revised form
22 September 2025
Accepted 23 September 2025
Available online 15 December 2025

Keywords:
Micromixing performance
Jet-stirred tank reactor
Computational fluid dynamics
Energy dissipation rate

ABSTRACT

To enhance the micromixing in chemical processes, a jet-stirred tank reactor (JSTR) was developed by integrating an annular jet with the width of 0.38 mm and 0.60 mm into a 81 L stirred tank to provide localized energy intensification. The iodide–iodate reaction method was used to evaluate the micromixing performance under different operating and structural conditions. Results showed that the micromixing time determined by the incorporation model decreased with increasing impeller speed and jet width, while the feeding position and jet velocity can significantly influence the micromixing due to jet deflection. The micromixing time in the JSTR ranged from 10 to 30 ms, representing a reduction of up to 3.45 times compared with the situation that only stirred tank was used. Numerical simulations of flow in the JSTR revealed four typical flow patterns illustrating the way by which the jet can affect the micromixing within the reactor. Furthermore, an operating diagram for mapping the micromixing time based on energy dissipation rate analysis was developed.
© 2025 The Chemical Industry and Engineering Society of China, and Chemical Industry Press Co., Ltd. All rights are reserved, including those for text and data mining, AI training, and similar technologies.

1. Introduction

Mixing is a critical unit operation in chemical processes, significantly affecting reaction efficiency and product quality. Based on the characteristic length scales, mixing is categorized into macromixing, mesomixing, and micromixing [1]. Macromixing distributes materials throughout the reactor *via* bulk flow, while mesomixing governs the breakup of large eddies and exchange between regions with different turbulence intensities. Micromixing is the final stage of homogenization, occurring on the molecular scale, which is at the same scale as chemical reactions [2]. It begins when the segregation scale reaches the Kolmogorov scale and proceeds to achieve molecular-level homogeneity primarily through molecular diffusion. Micromixing and intrinsic reaction kinetics jointly determine the reaction selectivity and product distribution. If micromixing time exceeds the characteristic reaction time, undesirable by-products may form in complex reactions. Therefore, micromixing is critical in many industrial processes, including polymerization [3], crystallization, and precipitation [4].

Given the sub-micrometer scales of micromixing, the molecular probe method is widely used to indirectly evaluate micromixing performance of the reactor. This approach infers reactor mixing conditions based on product composition and spatial distribution. Test systems include parallel competitive reactions (*e.g.*, iodide/iodate reactions [5,6], alkaline hydrolysis of ethyl chloroacetate [7]) and consecutive competing reactions (*e.g.*, diazo-coupling reaction [8]). Due to its high reaction rate, ease of detection, broad applicability, and low cost, the iodide–iodate system is the most widely used in micromixing studies [9,10].

Stirred tank reactors (STRs) are widely used in chemical processes for their operational flexibility and scalability [11]. In recent years, the micromixing optimization in STRs has primarily focused on impeller design. For example, Assirelli *et al.* [12] developed a modified Rushton turbine with rotating feeding pipes that reduced by-product formation compared to conventional feeding methods. Li *et al.* [13] investigated the effect of impeller diameter on the micromixing performance in aerated stirred tank equipped with half-elliptical blade-disc turbine and found that smaller impeller diameter enhances micromixing in single liquid systems but impedes it in gas–liquid systems. Yang *et al.* [14] developed a zigzag punched impeller generating impinging jet streams to disrupt the

This article is part of a special issue entitled: WCCE 12 & APCChE 2025 published in Chinese Journal of Chemical Engineering.

* Corresponding authors.
E-mail addresses: wangjunhao@buct.edu.cn (J. Wang), gaozm@mail.buct.edu.cn (Z. Gao).

https://doi.org/10.1016/j.cjche.2025.09.041
1004-9541/© 2025 The Chemical Industry and Engineering Society of China, and Chemical Industry Press Co., Ltd. All rights are reserved, including those for text and data mining, AI training, and similar technologies.

isolated zones, achieving better micromixing than standard impellers under the same power input. Liu *et al.* [15] numerically examined impeller combinations and found coaxial mixers with pitched-blade and Rushton turbines provided superior micromixing at a constant power.

Beyond impeller design, integrated reactor designs have shown potential for enhancing micromixing in STRs. Schaer *et al.* [16] demonstrated that jet velocity and positioning significantly affect micromixing performance when impinging jets are integrated into STRs. Wu *et al.* [17] developed a submerged circulative impinging stream reactor, achieving superior micromixing through high-velocity counter-current jet collisions. Other strategies, including the use of ultrasound [18,19], microfluidic stirrers [20], and propeller-driven torus reactors [21], have also been explored for micromixing enhancement.

Building upon the design of the impinging jet reactor [22], this study proposes a novel jet-stirred tank reactor (JSTR). The JSTR features a submerged upward jet beneath the impeller, generating a high-velocity upward flow that impinges on the impeller-induced downward flow, creating counter-current collisions in order to enhance micromixing near the jet exit. Firstly, the iodide–iodate reaction method was used to investigate the effects of impeller speed, jet velocity, feeding position, and jet width on micromixing performance. Then the numerical simulations were conducted to characterize the flow field and to clarify the way of mixing enhancement. In addition, an operating diagram was developed to predict micromixing time in the JSTR. This study aims to provide a systematic framework for understanding and optimizing micromixing in JSTRs, facilitating their application in rapid processes.

2. Experimental

2.1. The Villermaux/Dushman reaction method

The Villermaux/Dushman reaction is employed to characterize the micromixing performance of the JSTR. The parallel competitive reaction system consists of the following chemical reactions:

$$H_2BO_3^- + H^+ \rightarrow H_3BO_3 \quad (1)$$

$$5I^- + IO_3^- + 6H^+ \rightarrow 3I_2 + 3H_2O \quad (2)$$

$$I^- + I_2 \rightarrow I_3^- \quad (3)$$

Reaction (1) is quasi-instantaneous, while reaction (2) is fast but much slower in comparison. Reaction (3) is a quasi-instantaneous equilibrium reaction. The corresponding reaction rates and kinetic constants are listed in Table 1.

In this characterization reaction method, H_3BO_3 serves as the primary product, while I_2 is formed as a by-product. In the characterization of micromixing performance, a substoichiometric amount of acid is injected into a buffer solution containing $H_2BO_3^-$, I^-, and IO_3^-. Under perfect micromixing conditions, the limiting reactant H^+ is rapidly consumed by $H_2BO_3^-$ without generating additional by-products. However, under imperfect micromixing, H^+ becomes locally concentrated and is partially diverted to reaction (2), producing iodine I_2 and tri-iodide I_3^-. The concentration of I_3^-, quantified *via* UV spectrophotometry at 353 nm [1,6], follows a linear relationship with solution absorbance as governed by the Lambert–Beer law (Fig. 1):

$$[I_3^-] = \frac{D_{353}}{\gamma_{353} l} \quad (4)$$

where D_{353} is the light absorption of the I_3^- measured at 353 nm, γ_{353} is the molar extinction coefficient equal to 2586.5 $m^2 \cdot mol^{-1}$ and l is the optical path length equal to 0.01 m.

Generally, the segregation index, X_s, is used to quantify how perfect micromixing is in the reactor. The segregation index is defined as:

$$X_s = \frac{Y}{Y_{ST}} \quad (5)$$

$$Y = \frac{2(n_{I_2} + n_{I_3})}{n_{H_0^+}} = \frac{2(V_A + V_B)([I_2] + [I_3])}{V_B[H^+]_0} \quad (6)$$

$$Y_{ST} = \frac{6[IO_3^-]_0}{6[IO_3^-]_0 + [H_2BO_3^-]_0} \quad (7)$$

where Y is the ratio of the amount of H^+ consumed by reaction (2) to the total consumption, Y_{ST} is the value of Y in total segregation case, V_A is the volume of the buffer solution, and V_B is the volume of the acid solution. The segregation index can be ranged from 0 to 1, where $X_s = 0$ corresponds to a perfect micromixing and $X_s = 1$ represents total segregation (total imperfect micromixing).

2.2. Experimental setup

The structure details of the JSTR are shown in Fig. 2. Experiments were carried out in a flat-bottom plexiglass of internal diameter T_0 = 476 mm with a draft tube of internal diameter T_1 = 310 mm, and the liquid height H is kept at $H = T_0$. Five baffles were mounted circumferentially inside the draft tube to avoid the fluid whirling in the stirred tank. A five-blade axial-flow impeller (CBY) with a diameter of 300 mm was used to generate a strong downward axial flow inside the draft tube. The off-bottom clearance of the draft tube and the jet device were c_1 = 77.5 mm and

Table 1
Reaction rates and kinetic constants [23] of the test reaction system.

Reaction rate	Kinetic constant
$r_1 = k_1[H^+][H_2BO_3^-]$	$k_1 = 10^8\ m^3 \cdot mol^{-1} \cdot s^{-1}$
$r_2 = k_2[H^+]^2[IO_3^-][I^-]^2$	$k_2 = 10^{9.281-3.664\sqrt{I}}$, for $I < 0.16\ mol \cdot L^{-1}$
	$k_2 = 10^{8.383-1.511\sqrt{I}+0.2369I}$, for $I \geq 0.16\ mol \cdot L^{-1}$
$r_3 = k_3[I_2][I^-] - k_4[I_3^-]$	$k_3 = 5.9 \times 10^6\ m^3 \cdot mol^{-1} \cdot s^{-1}$
	$k_4 = 7.5 \times 10^6\ s^{-1}$

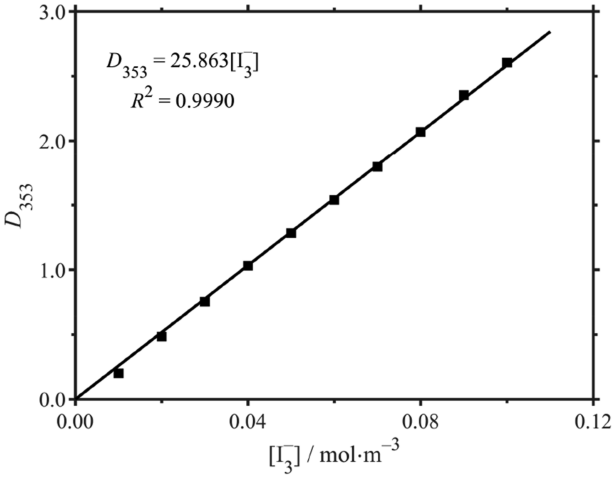

Fig. 1. Calibration curve for I_3^- absorbance.

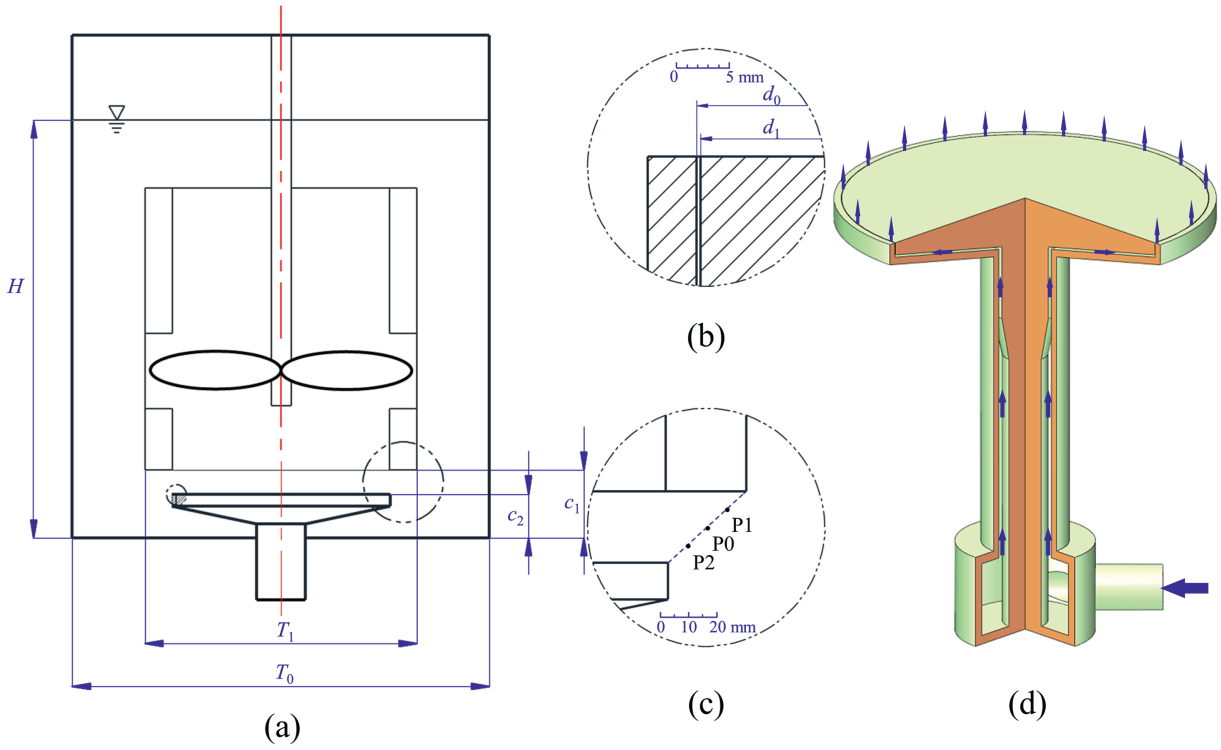

Fig. 2. Structural configuration and key dimensional of the JSTR: (a) reactor structure; (b) jet dimensions; (c) feeding position of the sulfuric acid; and (d) sectional view of annular jet.

$c_2 = 50$ mm, respectively. An annular jet exit design was adopted to enhance fluid dispersion within the reactor. The annular jet nozzle has a fixed outer diameter d_0 of 240.50 mm, with two interchangeable inner diameters d_1: 239.74 mm (jet width $w = 0.38 \pm 0.02$ mm) and 239.30 mm (jet width $w = 0.60 \pm 0.03$ mm). Three acid feeding positions were evenly spaced along the line connecting the jet exit to the lower edge of the draft tube, as shown in Fig. 2(c). The coordinates of the acid feeding positions are as follows: P0 ($r = 137.50$ mm, $z = 63.75$ mm), P1 ($r = 146.25$ mm, $z = 70.62$ mm), P2 ($r = 257.50$ mm, $z = 56.87$ mm). The key geometrical parameters of the JSTR are summarized in Table 2.

The schematic of the experimental setup is shown in Fig. 3. The reactor was initially filled with a premixed solution of KIO_3 (≥99.8%, Aladdin), KI (≥99%, Aladdin), H_3BO_3 (≥99.8%, Aladdin), and NaOH (≥98%, Aladdin), and the concentration of the reactant is shown in Table 3. The density and viscosity of the solution were 1000 kg·m^{-3} and 1 mPa·s, respectively. A total of 100 ml sulfuric acid solution was equally divided into five parts and injected into the JSTR through five capillaries with an internal diameter of 0.7 mm, which were uniformly arranged along the circumference inside the draft tube. This agreement matched the number of draft tube baffles, ensuring uniform placement between the baffles. The injection flow rate was accurately controlled by a micro-injection pump. The internal flow within the reactor was driven by both mechanical stirring and an external jet loop. The impeller generated a downward

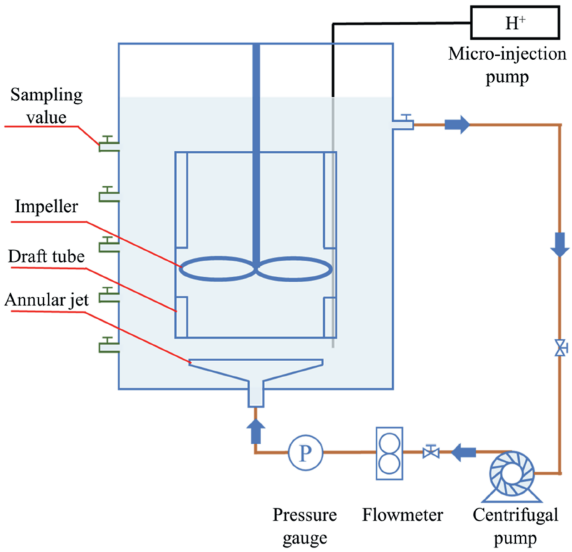

Fig. 3. Schematic diagram of experimental setup.

Table 2
Geometrical parameters of the JSTR.

Geometrical parameters	Value
Tank diameter, T_0/mm	476
Draft tube diameter, T_1/mm	310
Liquid height, H/mm	476
Impeller diameter/mm	300
Off-bottom clearance of the draft tube, c_1/mm	77.5
Off-bottom clearance of the jet device, c_2/mm	50
Outer diameter of the jet, d_0/mm	240.50
Inner diameter of the jet, d_1/mm	239.74 & 239.30
Jet width, w/mm	0.38 & 0.60

Table 3
Reactant concentrations (mol·L^{-1}).

KIO_3	KI	H_3BO_3	NaOH	H_2SO_4
0.00233	0.01165	0.1818	0.0909	0.5

flow through the draft tube, which then circulated along the outer wall and re-entered the draft tube from the top, forming an internal loop. At the same time, a portion of the liquid was withdrawn from the top of the reactor, passed through an external loop driven by the centrifugal pump, and was re-injected at the bottom *via* the annular jet. The upward jet interacted with the impeller-induced downward flow, enhancing local turbulence and micromixing near the feeding point. To minimize the influence of potential axial concentration gradients, solution samples were collected from five sampling ports at different heights after the reaction, and their absorbance was subsequently measured by a spectrophotometry (BlueStar A, Lab-Tech, China). Furthermore, the successive acid injection method [24] (one measurement per injection) was employed to reduce preparation time and experimental costs.

2.3. Experiment scheme

A series of experiments were designed to evaluate the effects of operating conditions and structural parameters on micromixing of the JSTR. The experimental conditions include the impeller speed (N), the jet velocity (v_{jet}), the acid feeding position, and the jet width (w). For each conditions, the experiments were repeated three times to ensure reproducibility, and the average value were used for futher analysis and discussion. The experimental conditions are summarized in Table 4 for ease of reference.

3. Numerical Simulation

3.1. Physical models and governing equations

Computational fluid dynamics provides an effective approach for investigating the internal flow characteristics within reactors. In this study, ANSYS Fluent was employed to analyze the flow behavior in the JSTR. Due to the complex geometry and the large disparity in characteristic length scales (0.1 mm at the jet exit *versus* 100 mm in the stirred tank), the computational domain was simplified to reduce simulation costs. The reactor geometry was azimuthally divided into five identical sectors, and periodic boundary conditions were applied, allowing the full reactor to be represented by a single sector. Since the internal flow within the jet device is not relevant to this study, only a representative segment immediately upstream of the jet exit was modeled to ensure a hydrodynamically fully developed flow entering the tank. To improve the resolution of the interaction between the jet and the stirring flow, the mesh near the jet exit was locally refined. The physical model and the surface mesh of the impeller and jet used in this study are shown in Fig. 4.

The simulation of incompressible fluid flow is based on the numerical solution of the continuity and Navier–Stokes equations, with the governing equations as shown below:

$$\nabla\cdot\boldsymbol{u}=0 \tag{8}$$

$$\rho\frac{\partial\boldsymbol{u}}{\partial t}+\rho\boldsymbol{u}\cdot\nabla\boldsymbol{u}=-\nabla p+\mu\nabla^2\boldsymbol{u}+\rho\boldsymbol{g} \tag{9}$$

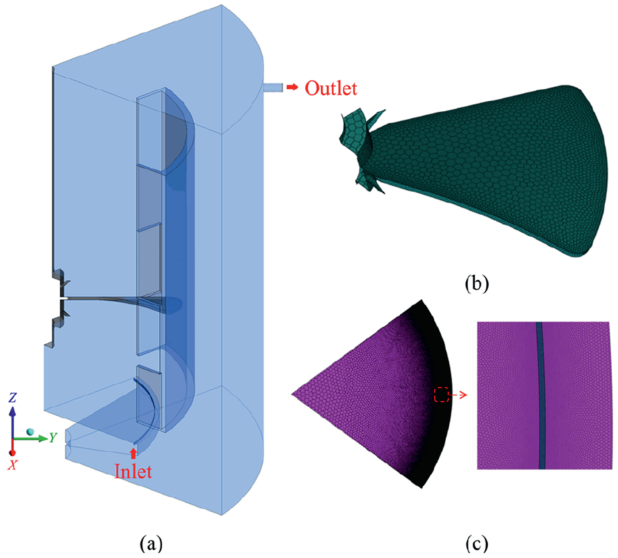

Fig. 4. Physical model and mesh for simulation: (a) physical model; (b) the surface mesh of the impeller; and (c) the surface mesh of the jet.

where $\boldsymbol{u}$ is the velocity, ρ is the density, p is the pressure, μ is the viscosity, and $\boldsymbol{g}$ is the gravitational acceleration vector.

The standard k–ε model was employed to close the turbulence equations. The transport equations for k and ε are expressed as follows:

$$\nabla\cdot(\rho\boldsymbol{u}k)=\nabla\cdot\left[\left(\mu+\frac{\mu_t}{\sigma_k}\right)\nabla k\right]+G_k-\rho\varepsilon \tag{10}$$

$$\nabla\cdot(\rho\boldsymbol{u}\varepsilon)=\nabla\cdot\left[\left(\mu+\frac{\mu_t}{\sigma_\varepsilon}\right)\nabla\varepsilon\right]+\frac{\varepsilon}{k}(C_{1\varepsilon}G_k-C_{2\varepsilon}\rho\varepsilon) \tag{11}$$

where the turbulent viscosity μ_t and the generation of turbulence kinetic energy due to the mean velocity gradients G_k are given by:

$$\mu_t=C_\mu\rho\frac{k^2}{\varepsilon} \tag{12}$$

$$G_k=\mu_t\sum_{i=1}^{3}\sum_{j=1}^{3}2\left(\frac{\partial u_i}{\partial x_j}+\frac{\partial u_j}{\partial x_i}\right)^2 \tag{13}$$

The model constants are as follows:

$$\sigma_k=1.0,\sigma_\varepsilon=1.3,C_{1\varepsilon}=1.44,C_{2\varepsilon}=1.92,C_\mu=0.09$$

3.2. Boundary conditions and simulation strategy

As this simulation focuses on steady, incompressible flow, ANSYS Fluent was employed with a pressure-based solver. The computational domain was divided into two regions: a rotating zone surrounding the impeller and a stationary zone containing the remaining parts of the JSTR. The Multiple Reference Frame

Table 4
Micromixing experimental conditions.

Impeller speed, N/r·min^{-1}	Jet velocity, v_{jet}/m·s^{-1}	Jet width, w/mm	Feeding position	Related section
31.8, 63.6, 95.4, 127.2, 159.0, 190.8, 222.6	0.5, 1.0, 1.5, 2.0, 2.5, 3.0, 3.5	0.38	P0	Section 4.2.2 & Section 4.2.3
95.4, 127.2	0.5, 1.0, 1.5, 2.0, 2.5, 3.0	0.38	P0, P1, P2	Section 4.2.4
95.4	0.5, 1.0, 1.5, 2.0	0.38, 0.60	P0	Section 4.2.5

approach was applied to model the rotating impeller. All wall boundaries were subjected to no-slip conditions. The pressure–velocity coupling was resolved using the Semi-Implicit Method for Pressure-Linked Equations algorithm. The second-order upwind scheme was adopted for the spatial discretization of all governing equations. Convergence was achieved when the residuals of all governing equations fell below 10^{-4}.

3.3. Grid independent verification

In numerical simulations, both the quality and density of the mesh are critical factors that significantly affect the accuracy of the computational results. Therefore, grid independence verification is essential. Three discretization schemes were evaluated, containing approximately 4.2 million, 5.4 million, and 7.0 million cells, respectively. Fig. 5 presents the velocity and turbulent kinetic energy distributions along the radial direction in the *yz*-plane at $z/H = 0.13$ under different grid resolutions. In the jet-affected region, the velocity profiles under the 5.4 million and 7.0 million cell meshes were nearly identical and both higher than those from the result of 4.2 million cell mesh. The turbulent kinetic energy exhibited a similar trend, indicating solution convergence with mesh refinement. Based on these results, the mesh with approximately 5.4 million cells was selected for all subsequent simulations to balance computational accuracy and cost.

4. Results and Discussion

4.1. Overall flow fields in the JSTR

In this study, flow fields were obtained by steady simulation. Fig. 6 presents the velocity fields in the *yz*-plane at an impeller speed of 95.4 rpm and a jet velocity of 3.0 m·s^{-1}. A typical circulating flow field is established in the reactor due to the use of the draft tube. Inside the draft tube, the down-pumping impeller drives the liquid downward along the axial direction, drawing liquid from the upper region of the tank into the impeller zone and thereby enhancing circulation and mixing. Subsequently, under the combined action of the jet and the impeller, the liquid flows upward through the annular space between the draft tube's outer wall and the reactor wall. Near the top of the reactor, the flow turns inward and re-enters the draft tube, completing the recirculation loop. Additionally, distinct jet diffusion and shear layers are

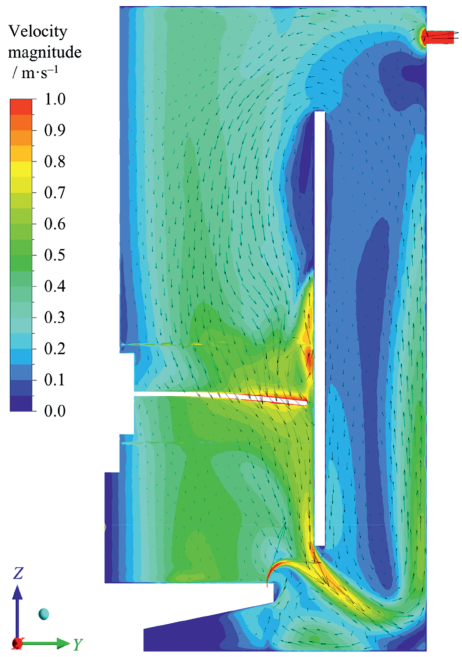

Fig. 6. Velocity fields in the *yz*-plane at $N = 95.4$ r·min^{-1} and $v_{jet} = 3.0$ m·s^{-1}.

observed near the jet exit. The jet stream increases the fluid velocity outside the draft tube and elevates the local shear rate near the jet, thereby enhancing mixing in this region.

4.2. Segregation index in the JSTR

4.2.1. Determination of feeding time

In micromixing experiments, the influence of macromixing on product distribution must be eliminated. Rapid acid injection can lead to poor acid dispersion, resulting in localized excess of H^+, and may also disturb the flow field near the feeding point. It is well accepted that a critical feeding time exists [6,14]. When the feeding time exceeds this critical value, X_s becomes independent of the feeding time and depends solely on micromixing performance. In this study, the feeding time of acid was determined at the lowest impeller speed (31.8 r·min^{-1}) and the lowest jet velocity (0.5 m·s^{-1}), corresponding to the worst macromixing condition. Fig. 7 illustrates that the segregation index stabilized when

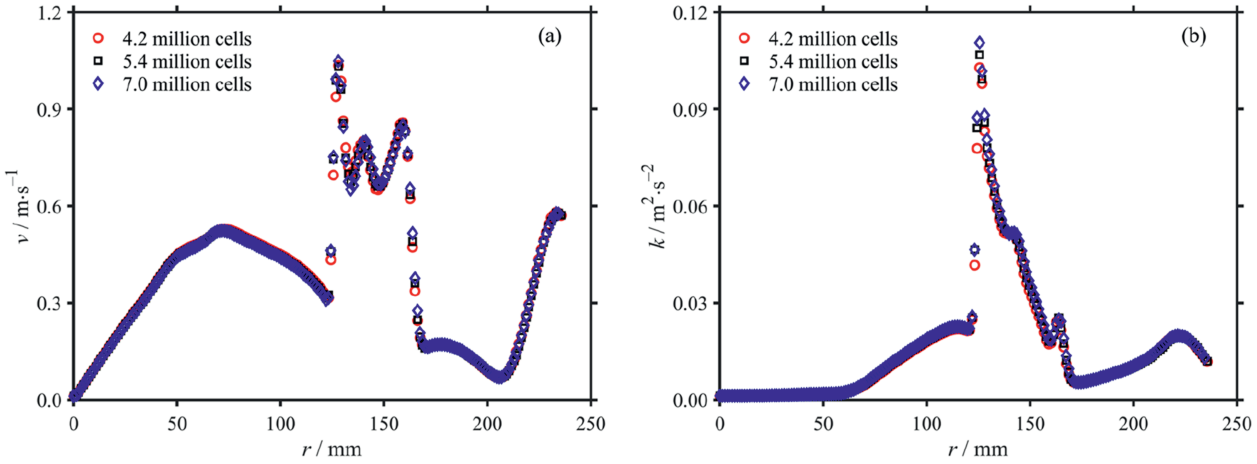

Fig. 5. Grid independence verification: distributions of (a) velocity magnitude and (b) turbulent kinetic energy on the *yz*-plane at $z/H = 0.13$ with 4.2 million, 5.4 million, 7.0 million cells, respectively ($N = 95.4$ r·min^{-1}, $v_{jet} = 3.0$ m·s^{-1}).

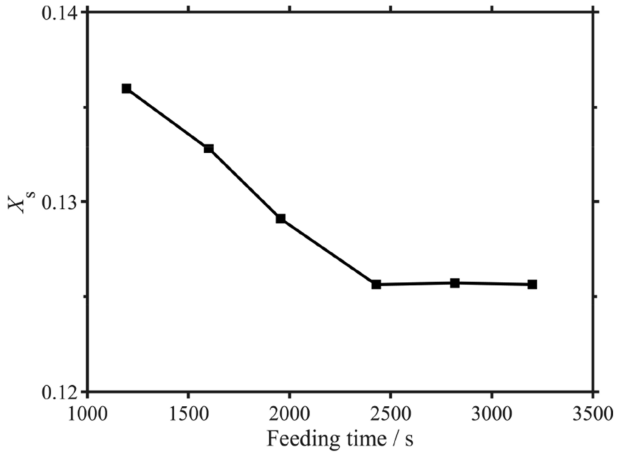

Fig. 7. Influences of acid feeding time on segregation index (N = 31.8 r·min^{-1}, v_{jet} = 0.5 m·s^{-1}, w = 0.38 mm feed at P0).

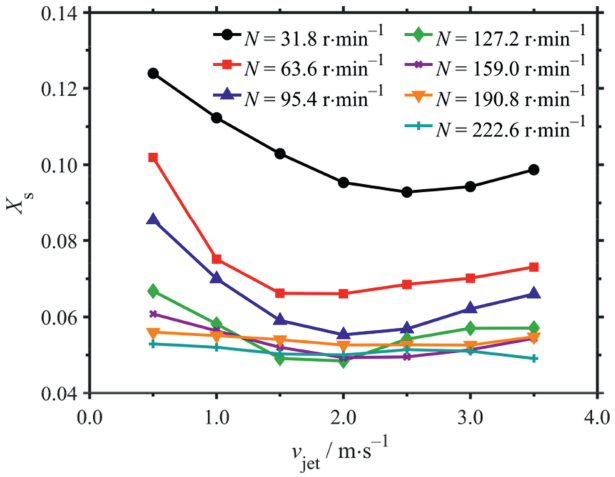

Fig. 9. Influences of jet velocity on segregation index (w = 0.38 mm, feed at P0).

the injection time exceeds 2400 s. Accordingly, a feeding time of 2800 s was selected for the subsequent experiments, corresponding to a feed flow rate of 0.43 ml·min^{-1}.

4.2.2. Effect of impeller speed

The impeller speed, as a key operating parameter in the JSTR, directly affects the turbulence intensity, shear rate, and interaction strength between the jet and the main flow, thereby influencing micromixing performance. The segregation index was measured at seven different impeller speeds, and the results are shown in Fig. 8. Experiments were repeated three times, and the maximum standard deviation observed was 0.57%, indicating good reproducibility.

As shown in Fig. 8, the segregation index decreases with increasing impeller speed, indicating enhanced micromixing performance at higher rotational speeds. This trend can be attributed to the increase in overall turbulence intensity within the reactor, which increases the local energy dissipation rate and improves the micromixing efficiency. The intensified turbulence promotes the rapid breakup and elongation of micro-scale fluid filaments, accelerating molecular diffusion and enhancing micromixing. In addition, Fig. 8 shows that the reduction in segregation index becomes less pronounced as the impeller speed increases. Two factors may explain this behavior. First, since the impeller power scales with the cube of the impeller speed, the relative increase in power and turbulence intensity are more significant at lower speeds for the same increment in impeller speed. Second, at sufficiently high impeller speeds, the micromixing time approaches the system's characteristic reaction time, reducing the sensitivity of the segregation index to further micromixing improvements. Consequently, the decline in segregation index with increasing impeller speed gradually plateaus.

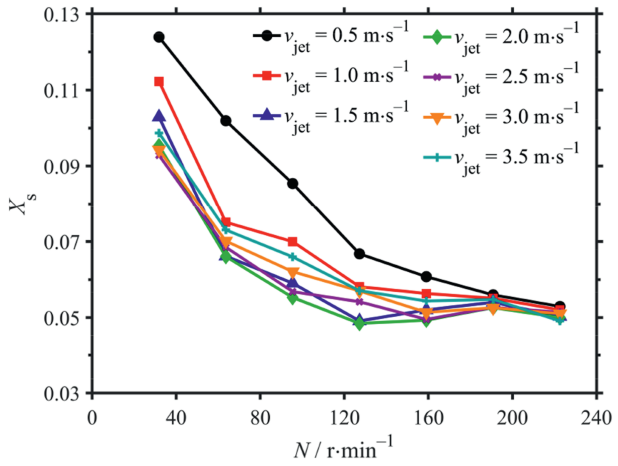

Fig. 8. Influences of impeller speed on segregation index (w = 0.38 mm, feed at P0).

4.2.3. Effect of jet velocity

Jet velocity is another critical operating parameter in the JSTR, directly influencing the turbulence intensity, jet penetration length, and the jet-stirring flow interaction. Fig. 9 shows the variation of the segregation index with jet velocity at different impeller speeds. Compared to the influence of impeller speed, the effect of jet velocity on the segregation index is more complex.

At low impeller speeds, the segregation index first decreases and then increases with increasing jet velocity. In contrast, at high impeller speeds, jet velocity has little effect on the segregation index. This behavior can be attributed to changes in the interaction between the jet and the stirring flow. Upon entering the reactor, the jet is deflected outward by the stirring flow, with its direction gradually changing from vertically upward to horizontal before merging with the bulk flow outside the draft tube.

It is important to note that parallel competitive reactions primarily occur near the feeding point, making the local energy dissipation rate in this region a determining factor for micromixing performance. At low impeller speeds and low jet velocities, the jet penetration length may be short and cannot reach the feeding point, resulting in minimal influence on local micromixing. As the jet velocity increases, the penetration length of jet increases, and its main development zone gradually extends toward the feeding point, enhancing local turbulence and shear and thereby improving micromixing. However, with further increases in jet velocity, the main development zone may move upward, leaving the feeding point below the jet's active region, which reduces local turbulence and increases the segregation index.

At high impeller speeds, the strong impeller-driven flow may limit the development of jet penetration and cause rapid breakup and dispersion of the jet, limiting its influence on local turbulence and micromixing near the feeding point. Consequently, jet velocity has little effect on the segregation index under these conditions.

4.2.4. Effect of acid feeding position

As mentioned earlier, the parallel competitive reactions occur mainly near the acid feeding point, making the injection position a

critical factor affecting product distribution. In this study, three feeding points were selected to study their effect on micromixing, with locations shown in Fig. 2(c). Due to the small characteristic size of the jet, the distances between the three injection points are shorter than other studies. Fig. 10 presents the segregation index curves for the different feeding positions.

As shown in Fig. 10, the segregation index exhibits significantly different trends with increasing jet velocity at the three feeding points. The results for P0 have been discussed previously in sections 4.2.2 and 4.2.3. At P1, the segregation index remains relatively constant at low jet velocities but decreases sharply with further increases in jet velocity, as shown in Fig. 10(b). This is because P1 is the farthest from the jet exit. At low jet velocities, the jet penetration length is insufficient to reach P1, resulting in negligible impact on local micromixing. As the jet velocity increases, the jet begins to affect micromixing at P1 by enhancing local turbulence and shear, thereby reducing the segregation index. Furthermore, the figure shows that higher impeller speeds correspond to higher jet velocities required for the segregation index to begin decreasing. This indicates that the effective jet penetration length influencing micromixing at P1 depends on both the impeller speed and the jet velocity. This observation is consistent with previous findings on jets entering regions with counter-current flow, where the jet penetration length is determined by the jet-to-counterflow velocity ratio [25].

At P2, the results in Fig. 10(c) show that the segregation index decreases continuously with increasing jet velocity. Since P2 is closest to the jet exit and located within the jet development zone, micromixing performance at P2 is predominantly controlled by the jet. As the jet velocity increases, local turbulence intensity is enhanced, leading to improved micromixing and a continuous reduction in the segregation index.

4.2.5. *Effect of jet width*

Jet width is a critical structural parameter that significantly influences the flow characteristics and micromixing performance within the JSTR. In this study, the jet width was varied by adjusting the inner diameter of the annular jet, and its effect on the segregation index was investigated at different jet velocities. As shown in Fig. 11, at the same jet velocity, increasing the jet width from 0.38 mm to 0.60 mm leads to a clear reduction in the segregation index, indicating a significant enhancement in micromixing efficiency.

This improvement can be attributed to several factors. At constant jet velocity, a larger jet width corresponds to a higher volumetric flow rate and greater momentum flux, generating stronger local disturbances that enhance the interaction between the jet and the bulk fluid driven by the impeller. The increased momentum input also promotes the rapid formation and stretching of small-scale eddies, accelerating turbulent diffusion. Additionally, a

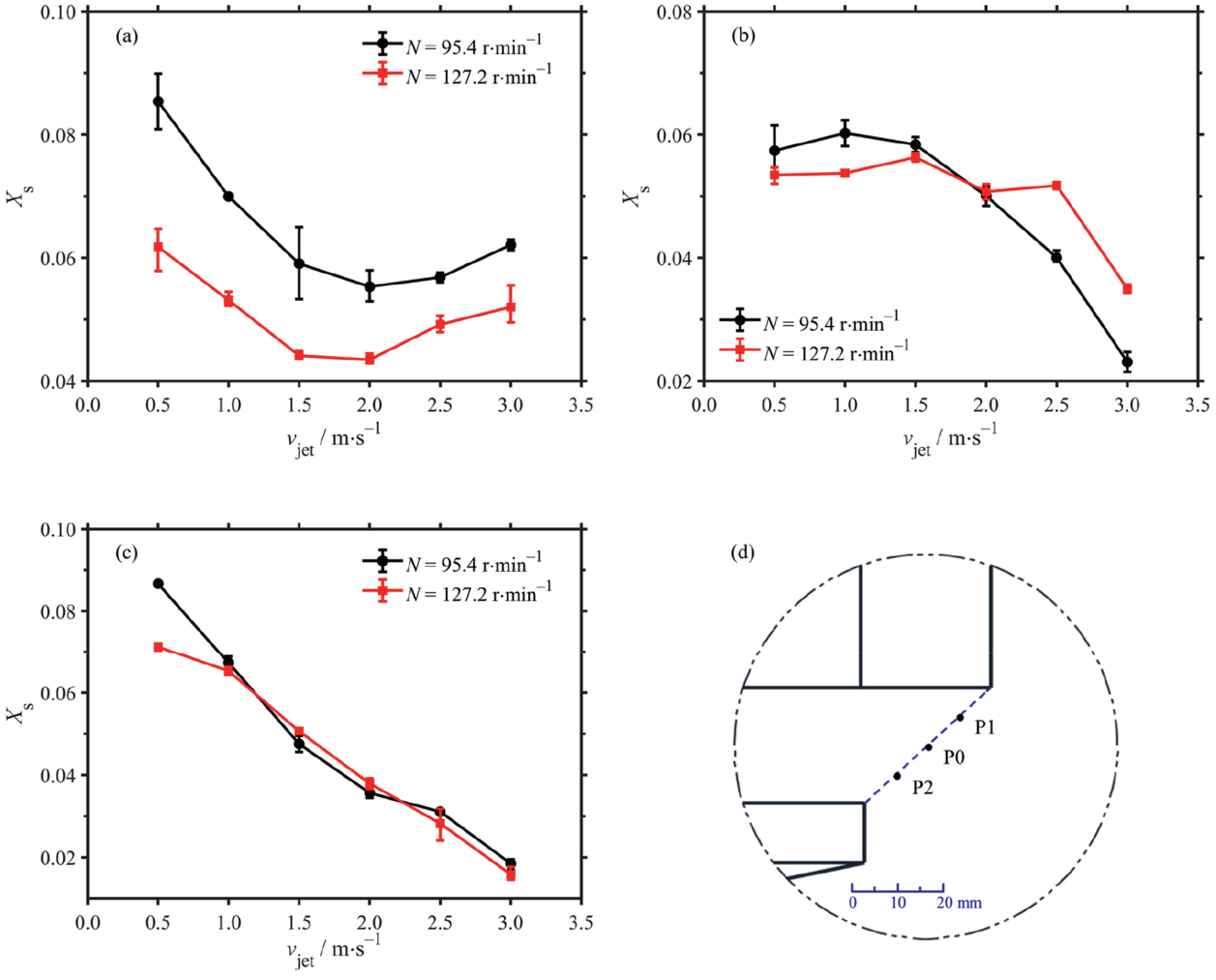

Fig. 10. Influences of feeding position on segregation index: (a) feed at P0; (b) feed at P1; (c) feed at P2; (d) feeding position (w = 0.38 mm).

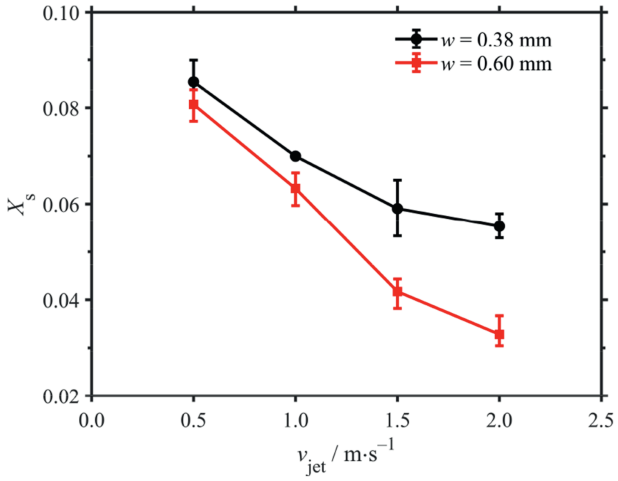

Fig. 11. Influences of jet width on segregation index (N = 95.4 r·min^{-1}, w = 0.38 mm, feed at P0).

wider jet expands the effective action area of the jet, increasing the probability of enhancing the turbulence intensity and energy dissipation rate near the feeding point. These combined effects improve the micromixing performance of the reactor, thereby reducing the segregation index.

4.2.6. Local flow fields in the JSTR

The flow in the JSTR can be complex due to the interaction between the jet and stirring flow. Fig. 12 presents four typical flow patterns, shown as velocity vectors and velocity magnitude contours in the *yz*-plane near the jet exit at an impeller speed of 95.4 r·min^{-1}. The black dot indicates the feeding point P0.

At low jet velocities (Fig. 12(a)), the jet fluid rapidly deflects upon entering the reactor and flows outward along the wall of the jet device. Under these conditions, the jet has a negligible influence on the overall flow field, and micromixing is primarily governed by impeller-induced turbulence with minimal contribution from the jet. As the jet velocity increases (Fig. 12(b)), the jet penetration length increases, altering the overall flow field. Although the jet still does not directly influence micromixing near the injection point, the increased jet penetration length constricts the fluid path from the interior to the exterior of the draft tube. This constriction increases the local fluid velocity near the feeding point, enhancing turbulence intensity and shear rate, which improves micromixing efficiency in this region. At higher jet velocities (Fig. 12(c)), the jet core directly penetrates the feeding point, significantly increasing local turbulence intensity and energy dissipation. Under these conditions, the reactor achieves optimal micromixing performance due to the enhanced turbulence and energy dissipation. However, when the jet velocity exceeds this optimum, the penetration length continues to increase, causing the distance between the jet core and the feeding point to increase.

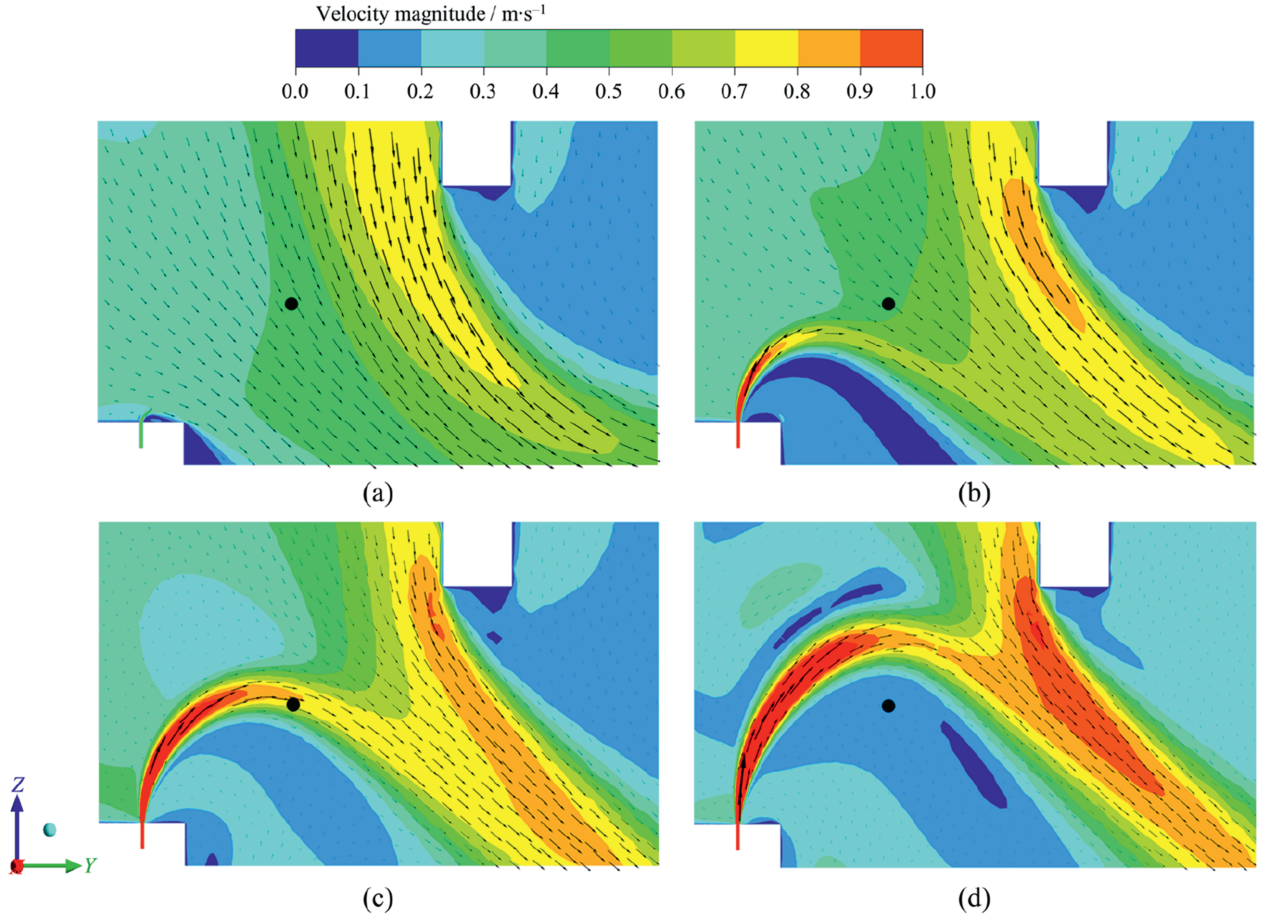

Fig. 12. Simulated velocity fields in the *yz*-plane at N = 95.4 r·min^{-1} and (a) v_{jet} = 0.5 m·s^{-1}; (b) v_{jet} = 2.0 m·s^{-1}; (c) v_{jet} = 3.0 m·s^{-1}; (d) v_{jet} = 4.0 m·s^{-1}.

This leads to a reduction of local turbulence intensity at the feeding point and a decline in micromixing efficiency. At excessively high jet velocities (Fig. 12(d)), the feeding point becomes engulfed in a low-viscosity zone formed by jet deflection, resulting in severely degraded micromixing performance.

4.3. Relationship between the segregation index and micromixing time

As a dimensionless parameter derived from competitive reaction systems, the segregation index serves as a sensitive indicator of micromixing efficiency. However, due to the absence of a clear physical time dimension, it cannot be directly correlated with the characteristic reaction time of the chemical reaction. To address this limitation, it is necessary to establish a model relating the X_s to the t_m. Several models have been proposed to estimate the micromixing time based on the segregation index, such as IEM model (interaction by exchange with the mean model) [26], incorporation model [27], and engulfment model [28,29]. Among these, the incorporation model is widely used due to its simplicity and its effectiveness in accurately describing micromixing behavior across various types of reactors [12,30,31]. Therefore, in this study, the incorporation model was adopted to establish the quantitative relationship between the segregation index and the micromixing time in the JSTR.

In the incorporation model applied to the Villermaux/Dushman test reaction, it is assumed that the injected acid is initially divided into a large number of aggregates dispersed in the bulk fluid. The bulk fluid, containing iodide, iodate, and the borate buffer, progressively invades these acid aggregates through entrainment and molecular diffusion. The reactions occur only within the acid aggregates. The volume of these aggregates increases over time according to the incorporation model, with the growth rate governed by the micromixing process. The characteristic incorporation time obtained from this model is commonly used as an estimate of the micromixing time under given operating conditions. In the aggregates, the concentrations of species j evolve according to:

$$\frac{dC_j}{dt} = \frac{\left(C_{j,1,0} - C_j\right)}{V_2}\frac{dV_2}{dt} + r_j \tag{14}$$

where subscript 0 denotes the initial state, subscript 1 refers to the bulk fluid, and subscript 2 corresponds to the aggregates. V_2 represents the volume of the aggregates, and r_j denotes the reaction rates.

In this study, the incomplete dissociation of sulfuric acid was also considered by including the following two dissociation reactions:

$$H_2SO_4 \rightarrow H^+ + HSO_4^- \tag{15}$$

$$HSO_4^- \rightarrow H^+ + SO_4^{2-} \tag{16}$$

By assuming a series of initial value for t_m and solving Eq. (14), the product concentration required to calculate the segregation index was obtained. Consequently, the relationship between t_m and X_s, as illustrated in Fig. 13, was established. The micromixing time of the JSTR ranges from 10 to 30 ms under the experimental conditions. For quantitative comparison, experiments were also conducted with $v_{jet} = 0$, representing a conventional STR, where the micromixing time ranged from 11 to 133 ms. Table 5 summarizes the micromixing times of the JSTR and the STR at same impeller speeds. Under low impeller speed conditions, the micromixing time in the JSTR was reduced by up to 77%. For certain fast reactions, such as polymerization and precipitation, the products are sensitive to shear forces, which limits the maximum impeller speed of the conventional STRs. In such cases, integrating a jet device can effectively improve the local micromixing performance within the reactor.

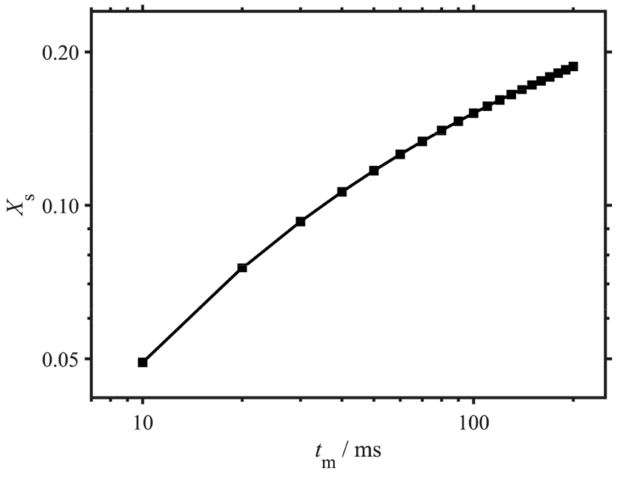

Fig. 13. Relationship between the segregation index and micromixing time.

4.4. Modelling of micromixing time in the JSTR

Accurate prediction and control of the t_m are essential for optimizing reactors handling fast reaction systems, ensuring consistent product quality. To enable the prediction of t_m, it is necessary to develop a method for calculating t_m based on operating parameters. According to turbulent micromixing theory [1], the micromixing time t_m is given by:

$$t_m = \alpha\left(\frac{\nu}{\varepsilon}\right)^{0.5} \tag{17}$$

where ν is the fluid kinematic viscosity, ε is the energy dissipation rate, and α is an empirical constant. Consequently, determining

Table 5
Comparison of micromixing time of JSTR and STR ($w = 0.38$ mm, feed at P0).

Impeller speed/r·min^{-1}	$t_{m,JSTR}$/ms	$t_{m,STR}$/ms	$\frac{t_{m,STR} - t_{m,JSTR}}{t_{m,STR}} \times 100\%$
31.8	29.9	133.3	77.57%
63.6	15.9	43.2	63.18%
95.4	13.7	25.7	46.72%
127.2	9.8	17.6	44.47%
159.0	10.0	14.2	29.38%
190.8	11.1	13.0	14.86%
222.6	10.0	11.4	12.39%

the local energy dissipation rate under various operating conditions in the JSTR is crucial for reliably predicting the micromixing time.

The flow patterns within the JSTR are complex, with the local energy dissipation rate influenced by both the impeller and the jet flow fields. Therefore, the energy dissipation rates contributions from the jet and the impeller can be calculated separately and then correlated with t_m in the JSTR.

4.4.1. Local energy dissipation rate of the impeller

In a fully turbulent stirred tank reactor, the local energy dissipation rate is proportional to the average energy dissipation rate of the reactor [16]:

$$\varepsilon_i = \phi_i \overline{\varepsilon_i} \tag{18}$$

where ϕ_i is the proportionality constant. In this study, the ϕ_i value at P0 was determined using numerical simulations. By simulating the JSTR with $v_{jet} = 0$, the impeller torque, τ, and the local energy dissipation rate near P0, $\varepsilon_{i,sim}$, were obtained. According to Eqs. (19) and (20), the ϕ_i value was calculated to be 1.92 based on the simulation results. Related simulation data are provided in Supplementary Material.

$$\overline{\varepsilon_{i,sim}} = \frac{P_{i,sim}}{\rho V_{sim}} = \frac{2\pi N\tau}{\rho V_{sim}} \tag{19}$$

$$\phi_i = \frac{\varepsilon_{i,sim}}{\overline{\varepsilon_{i,sim}}} \tag{20}$$

where ρ is the fluid density, V_{sim} is the simulated reactor volume, equal to 1/5 of the total fluid volume in the reactor V_m, as mentioned in section 3.1.

In the experiment, the average energy dissipation rate in the stirred tank reactor can be calculated as:

$$\overline{\varepsilon_i} = \frac{P_i}{\rho V_m} = N_p \frac{N^3 D^5}{V_m} \tag{21}$$

where N_p is the power number, N is the impeller speed, D is the impeller diameter, and V_m is the volume of the fluid in the reactor. Based on experiment tests, the power number (N_p) of the impeller used present work was determined to be 1.10.

4.4.2. Local energy dissipation rate of the jet

As there are currently no reported studies on the local energy dissipation rate of jets within the JSTR, this study employed the local energy dissipation rate of a free jet to estimate the jet's contribution to micromixing in the JSTR. Given that the ring diameter of the annular jet is much larger than the width, the jet can be regarded as a plane jet. The schematic of a free plane jet is shown in Fig. 14.

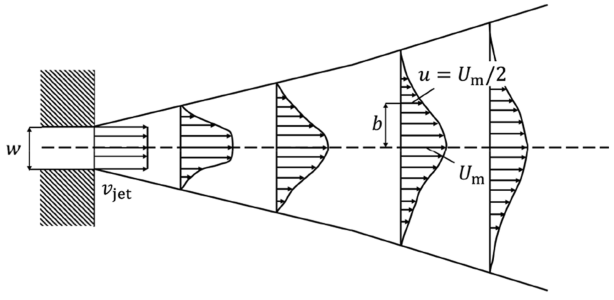

Fig. 14. Schematic of the development of a free plane jet.

According to phenomenological turbulence theory [32], the mean energy dissipation rate ε can be expressed as:

$$\varepsilon \propto \frac{u_0^3}{l_0} \tag{22}$$

where u_0 and l_0 represent the characteristic velocity and length scales of the large turbulent eddies. In free jets, the characteristic velocity u_0 can be taken as the local maximum mean streamwise velocity along the jet centerline, denoted as U_m. Similarly, the characteristic length scale l_0 can be represented by the local half-width of the jet, b, defined as the lateral distance from the centerline where the mean streamwise velocity decreases to $U_m/2$. In the self-preserving region of a plane jet, the local maximum mean streamwise velocity U_m and the local half-width b can be expressed as:

$$U_m \propto v_{jet}\left(\frac{x}{w}\right)^{-\frac{1}{2}} \tag{23}$$

$$b \propto x \tag{24}$$

where v_{jet} represent the velocity at the jet exit, x is the straight-line distance from the jet exit (in mm). Therefore, the local energy dissipation rate in a free plane jet can be expressed as:

$$\varepsilon_j = \phi_j v_{jet}^3 x^{-\frac{5}{2}} w^{\frac{3}{2}} \tag{25}$$

From the numerical simulation under the condition of $N = 0$ in the JSTR (related simulation data are provided in Supplementary Material), the ϕ_j was empirically determined to be a function of x:

$$\phi_j = 0.0013x^2 - 0.085x + 2.4 \quad (10\ \text{mm} < x < 50\ \text{mm}) \tag{26}$$

The free-jet assumption employed in this study is applicable when the feeding point is located near and downstream of the jet exit, and when the jet velocity is sufficiently high to allow proper development. In cases of strong interaction with the impeller-induced counterflows and crossflow, the local energy dissipation rate may be higher than predicted and the model could slightly underestimate the dissipation [25,33].

4.4.3. Operating diagram of the JSTR

Based on the experimental data, the operating diagram of the JSTR were constructed, as shown in Fig. 15, where the contour

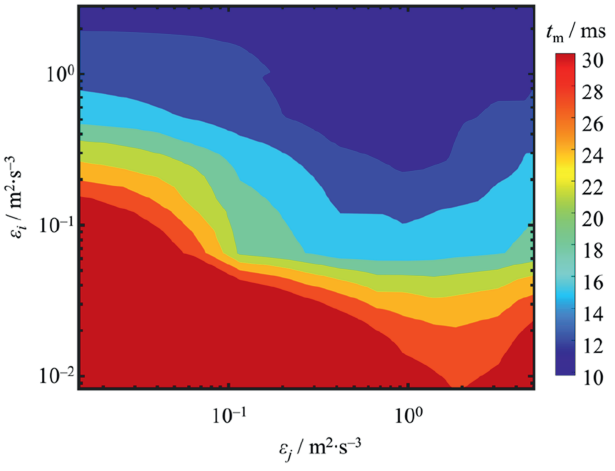

Fig. 15. Operating diagram of the JSTR for micromixing time mapping.

represents the predicted micromixing time. In the JSTR, the energy dissipation rates contributed by the jet and the impeller can be estimated from the operating conditions. By correlating these values with the operating diagram, the micromixing time within the JSTR can be predicted and mapped, enabling a quantitative assessment of the micromixing performance under various conditions. Furthermore, when designing a JSTR to meet specific industrial micromixing time requirements, the operating diagram can be employed to identify the necessary combination of the jet and impeller energy dissipation rates. This approach provides practical guidance for selecting and designing operating conditions in JSTRs to achieve the desired micromixing performance.

5. Conclusions

This study proposed a novel jet-stirred tank reactor (JSTR) to intensify the micromixing in chemical processes. The effects of operating and structural conditions on micromixing performance of the JSTR were investigated using the iodide-iodate reaction method. Experimental results show that segregation index decreases with increasing impeller speed and jet width. Jet velocity primarily influences micromixing by altering the jet penetration length. At low impeller speeds, the segregation index initially decreases and then increases with the increase of jet velocity. While at high impeller speeds, the segregation index remains relatively stable regardless of jet velocity. Micromixing efficiency at different feeding positions is governed by stirring flow, jet flow, or their combination. Based on the incorporation model, the micromixing time of the JSTR ranges from 10 to 30 ms, achieving reductions of up to 77% compared to STRs, particularly at low impeller speeds. Numerical simulations reveal the complex interaction between the jet and the stirring fluid, indicating that micromixing performance is significantly enhanced within an optimal jet velocity range, beyond which micromixing performance is limited or even degraded. Compared to conventional STRs, the jet provides a concentrated source of energy within the JSTR. This feature makes the JSTR well-suited for rapid, shear-sensitive processes that require intense mixing during the initial contact of reactants. Primary application areas include fast chemical reactions such as precipitation and crystallization of fine chemicals and pharmaceuticals, polymerization processes requiring precise control of molecular weight distribution, and nanoparticle synthesis where a narrow size distribution is desired.

To support the practical application of this research, an operating diagram was developed based on the analysis of impeller and jet energy dissipation rates. This diagram enables the estimation of micromixing time across various operating and structural configurations, serving as a valuable tool for evaluating the micromixing characteristic of JSTR and the designing of operational parameters.

CRediT Authorship Contribution Statement

Guangshuo Wu: Writing — original draft, Methodology, Investigation. Ziqi Cai: Resources, Investigation, Funding acquisition. Zhipeng Li: Supervision, Funding acquisition. Junhao Wang: Writing — review & editing, Supervision. Zhengming Gao: Supervision, Funding acquisition, Data curation.

Declaration of Competing Interest

The authors declare that they have no known competing financial interests or personal relationships that could have appeared to influence the work reported in this paper.

Acknowledgements

The authors gratefully acknowledge the financial support from the China Petrochemical Corporation (Sinopec Group, project number: 222129, 224285, and 224108).

Nomenclature

b	distance between the point with velocity $U_m/2$ to the centreline, mm
C_j	concentration of species j, $mol \cdot m^{-3}$
c_1	off-bottom clearance of the draft tube, mm
c_2	off-bottom clearance of the jet device, mm
D	impeller diameter, mm
D_{353}	light absorption
d_0	outer diameter of the jet, mm
d_1	inner diameter of the jet, mm
$\boldsymbol{g}$	gravitational acceleration vector, $m \cdot s^{-2}$
H	liquid height, mm
k	turbulent kinetic energy, $m^2 \cdot s^{-2}$
k_1	kinetic constant of reaction (1), $m^3 \cdot mol \cdot s^{-1}$
k_2	kinetic constant of reaction (2), $m^{12} \cdot mol^{-4} \cdot s^{-1}$
k_3	kinetic constant of reaction (3), $m^3 \cdot mol \cdot s^{-1}$
k_4	reverse kinetic constant of reaction (3), s^{-1}
N	impeller speed, $r \cdot min^{-1}$
N_p	power number
p	pressure of the fluid, Pa
r_1, r_2, r_3	reaction rate, $mol \cdot m^{-3} \cdot s^{-1}$
r_j	reaction rates of species j, $mol \cdot m^{-3} \cdot s^{-1}$
T_0	tank diameter, mm
T_1	draft tube diameter, mm
t_m	micromixing time, ms
U_m	local maximum mean streamwise velocity of the jet, $m \cdot s^{-1}$
$\boldsymbol{u}$	vector of velocity, $m \cdot s^{-1}$
V_A	volume of the buffer solution, m^3
V_B	volume of the acid, m^3
v_{jet}	velocity of the jet, $m \cdot s^{-1}$
w	width of the jet, mm
X_s	segregation index
x	the distance from the jet exit, mm
Y	actual yield of undesired product
Y_{ST}	value of Y in the total segregation
ε	energy dissipation rate, $m^2 \cdot s^{-3}$
γ_{353}	molar extinction coefficient, $m^2 \cdot mol^{-1}$
μ	viscosity of fluid, $Pa \cdot s$
ν	kinematic viscosity, $m^2 \cdot s^{-1}$
ρ	density of fluid, $kg \cdot m^{-3}$
τ	torque of the impeller, $N \cdot m^{-1}$

Supplementary Material

Supplementary data to this article can be found online at https://doi.org/10.1016/j.cjche.2025.09.041.

References

[1] A. Nie, Z.M. Gao, L. Xue, Z.Q. Cai, G.M. Evans, A. Eaglesham, Micromixing performance and the modeling of a confined impinging jet reactor/high speed disperser, *Chem. Eng. Sci.* 184 (2018) 14–24.
[2] J. Bałdyga, R. Pohorecki, Turbulent micromixing in chemical reactors — a review, *Chem. Eng. J. Biochem. Eng. J.* 58 (2) (1995) 183–195.
[3] Y. Song, M. Shang, G. Li, Z.H. Luo, Y. Su, Influence of mixing performance on polymerization of acrylamide in capillary microreactors, *AIChE J* 64 (5) (2017) 1828–1840.
[4] H.K. Chan, P.C. Kwok, Production methods for nanodrug particles using the bottom-up approach, *Adv. Drug Deliv. Rev.* 63 (6) (2011) 406–416.

[5] P. Guichardon, C. Baqueiro, N. Ibaseta, Villermaux–Dushman test of micromixing characterization revisited: kinetic effects of acid choice and ionic strength, *Ind. Eng. Chem. Res.* 60 (50) (2021) 18268–18282.
[6] M.C. Fournier, L. Falk, J. Villermaux, A new parallel competing reaction system for assessing micromixing efficiency—experimental approach, *Chem. Eng. Sci.* 51 (22) (1996) 5053–5064.
[7] R. King, Fluid Mechanics of Mixing: Modelling, Operations and Experimental Techniques. Springer, Netherlands, (1992).
[8] J.R. Bourne, F. Kozicki, P. Rys, Mixing and fast chemical reaction—I: test reactions to determine segregation, *Chem. Eng. Sci.* 36 (10) (1981) 1643–1648.
[9] D. Wang, Y. Qiu, Z. Chen, C. Gu, X. Ling, H. Peng, X. Yang, F. Yuan, J. Du, W. Yu, Characterization of micromixing intensification of impinging jet flow on a spinning disk reactor with a structured surface, *Ind. Eng. Chem. Res.* 63 (24) (2024) 10782–10794.
[10] Y. Ouyang, M.N. Manzano, K. Beirnaert, G.J. Heynderickx, K.M. van Geem, Micromixing in a gas–liquid vortex reactor, *AIChE J.* 67 (7) (2021) e17264.
[11] F. Visscher, J. van der Schaaf, T.A. Nijhuis, J.C. Schouten, Rotating reactors—a review, *Chem. Eng. Res. Des.* 91 (10) (2013) 1923–1940.
[12] M. Assirelli, E.J.W. Wynn, W. Bujalski, A. Eaglesham, A.W. Nienow, An extension to the incorporation model of micromixing and its use in estimating local specific energy dissipation rates, *Ind. Eng. Chem. Res.* 47 (10) (2007) 3460–3469.
[13] W. Li, X. Geng, Y. Bao, Z. Gao, Micromixing characteristics in the impeller discharging area in aerated stirred tank, *J. Chem. Eng. Jpn.* 46 (11) (2013) 717–725.
[14] J. Yang, Q. Zhang, Z.-S. Mao, C. Yang, Enhanced micromixing of Non-Newtonian fluids by a novel zigzag punched impeller, *Ind. Eng. Chem. Res.* 58 (16) (2019) 6822–6829.
[15] B. Liu, N. Sun, Z. Jin, Y. Zhang, B. Sunden, Numerical investigation and estimating correlation of micromixing performance of coaxial mixers, *Ind. Eng. Chem. Res.* 58 (49) (2019) 22376–22388.
[16] E. Schaer, P. Guichardon, L. Falk, E. Plasari, Determination of local energy dissipation rates in impinging jets by a chemical reaction method, *Chem. Eng. J.* 72 (2) (1999) 125–138.
[17] Y. Wu, Y. Xiao, Y. Zhou, Micromixing in the submerged circulative impinging stream reactor, *Chin. J. Chem. Eng.* 11 (4) (2003) 54–59.
[18] H. Monnier, A.M. Wilhelm, H. Delmas, The influence of ultrasound on micromixing in a semi-batch reactor, *Chem. Eng. Sci.* 54 (13-14) (1999) 2953–2961.
[19] J. Jordens, B. Bamps, B. Gielen, L. Braeken, T. van Gerven, The effects of ultrasound on micromixing, *Ultrason. Sonochem.* 32 (2016) 68–78.
[20] S.D. Qin, J.F. Zhang, J. Zhang, D.B. Zhao, X. Xu, D.C. Jiang, Study on mixing performance of high-viscosity fluid in continuous microfluidic multistage stirrer, *Ind. Eng. Chem. Res.* 64 (12) (2025) 6407–6419.
[21] L.h. Nouri, J. Legrand, N. Benmalek, F. Imerzoukene, A.-R. Yeddou, F. Halet, Characterisation and comparison of the micromixing efficiency in torus and batch stirred reactors, *Chem. Eng. J.* 142 (1) (2008) 78–86.
[22] Z. Gao, J. Han, Y. Xu, Y. Bao, Z. Li, Particle image velocimetry (PIV) investigation of flow characteristics in confined impinging jet reactors, *Ind. Eng. Chem. Res.* 52 (33) (2013) 11779–11786.
[23] P. Guichardon, L. Falk, J. Villermaux, Characterisation of micromixing efficiency by the iodide–iodate reaction system. Part II: kinetic study, *Chem. Eng. Sci.* 55 (19) (2000) 4245–4253.
[24] P. Guichardon, L. Falk, Characterisation of micromixing efficiency by the iodide–iodate reaction system. Part I: experimental procedure, *Chem. Eng. Sci.* 55 (19) (2000) 4233–4243.
[25] Z. Li, Y. Xiao, W. Huai, L. Ding, Velocity characteristics of a round offset jet with different offset ratios in a counterflow, *Flow Turbul. Combust.* 107 (1) (2020) 81–104.
[26] J. Villermaux, R. David, Recent advances in the understanding of micromixing phenomena in stirred reactors, *Chem. Eng. Commun.* 21 (1-3) (1983) 105–122.
[27] M.C. Fournier, L. Falk, J. Villermaux, A new parallel competing reaction system for assessing micromixing efficiency—determination of micromixing time by a simple mixing model, *Chem. Eng. Sci.* 51 (23) (1996) 5187–5192.
[28] J. Baldyga, J.R. Bourne, Simplification of micromixing calculations. II. New applications, *Chem. Eng. J.* 42 (2) (1989) 93–101.
[29] J. Baldyga, J.R. Bourne, Simplification of micromixing calculations. I. Derivation and application of new model, *Chem. Eng. J.* 42 (2) (1989) 83–92.
[30] E. Arian, W. Pauer, Contributions to the kinetics of the iodide-iodate test reaction for micromixing time calculation with extended incorporation models, *Chem. Eng. Sci.* 237 (2021) 116549.
[31] H. Ye, J. Guo, X. Li, R. Chi, B. Long, Y. Han, W. Li, J. Wu, J. Zhang, Improving the accuracy of micromixing time using Villermaux–Dushman reaction with incorporation model, *Chem. Eng. Sci.* 306 (2025) 121254.
[32] R.A. Antonia, B.R. Satyaprakash, A.K.M.F. Hussain, Measurements of dissipation rate and some other characteristics of turbulent plane and circular jets, *Phys. Fluids* 23 (4) (1980) 695–700.
[33] K. Mahesh, The interaction of jets with crossflow, *Annu. Rev. Fluid Mech.* 45 (1) (2013) 379–407.